Chapter 12: Fundamental Concepts for Impedance-based Structural Health Monitoring

Chapter details

Chapter DOI:

https://doi.org/10.4322/978-65-86503-71-5.c12

Chapter suggested citation / reference style:

Finzi Neto, Roberto M., Moura Junior, Jose R. V. (2022). "Fundamental Concepts for Impedance-based Structural Health Monitoring". *In* Jorge, Ariosto B., et al. (Eds.) *Model-Based and Signal-Based Inverse Methods*, Vol. I, UnB, Brasilia, DF, Brazil, pp. 443–471. Book series in Discrete Models, Inverse Methods, & Uncertainty Modeling in Structural Integrity.

P.S.: DOI may be included at the end of citation, for completeness.

Book details

Book: Model-based and Signal-Based Inverse Methods

Edited by: Jorge, Ariosto B., Anflor, Carla T. M., Gomes, Guilherme F., & Carneiro, Sergio H. S.

Volume I of Book Series in:

Discrete Models, Inverse Methods, & Uncertainty Modeling in Structural Integrity

Published by: UnB City: Brasilia, DF, Brazil Year: 2022

DOI: https://doi.org/10.4322/978-65-86503-71-5

Fundamental Concepts for Impedance-based Structural Health Monitoring

Roberto Mendes Finzi Neto*[1], Jose dos Reis Vieira de Moura Junior[2]

[1]Post-Graduate Program – Mechanical Engineering, Fed. University of Uberlandia, Brazil. E-mail: finzi@ufu.br
[2]Post-Graduate Program – Modeling and Optimization, Fed. University of Catalao, Brazil. E-mail: zereis@ufcat.edu.br

*Corresponding author

Abstract

Engineering has developed new approaches over the last 50 years in all its areas. Among the different areas, the design areas became more agile and computer-based, logistics developed new modes and interactions more Just in Time, while materials engineering revolutionized the options of possibilities in all sectors. However, the maintenance area gains special attention due to its objective to present limiting working conditions. While the production areas allow infinite productivity development, creating new processes and techniques, the maintenance area has a limit of improvement focused on the utopian zero defects. Thus, several techniques have been developed in recent decades, mainly with the advancement of computational power and integration. Techniques for assessing structural integrity have also developed, enabling the implementation of more precise techniques in the qualitative capacity of identifying a failure, as well as quantifying its severity and location. This chapter discusses the Structural Integrity Monitoring Method based on Electromechanical Impedance. This is one of the most explored techniques in recent decades by several research groups in Brazil and worldwide, having applications in aeronautics, space, oil and gas, bioengineering, civil construction, among others. In the next sections, some historical aspects of the technique are presented, as well as basic concepts and variables that influence this monitoring. Finally, a case study of the investigation of a failure simulated by machining an aluminum structure monitored in a climatic chamber is presented. As it is a chapter in which it is more concerned with the fundamentals and aspects that influence the use of the methodology, the conclusions of this case study do not cover any type of statistical modeling or based on machine learning as usually seen in scientific articles in the method. In this case, the effects of temperature on the impedance signature are focused, as well as the calculation of some damage metrics.

1. Introduction of the Impedance-based SHM

The SHM method described in this section is based on the electromechanical impedance (EMI), an ultrasonic technique that has been considered one of the most attractive nondestructive methods (NDE) for evaluating different types of structures.

The Impedance-based SHM technique (ISHM) was first proposed by Liang *et al*. (1994) and, subsequently, the method was extended by Chaudhry *et al*. (1995, 1996), Sun *et al*. (1995), Park *et al.* (1999, 2000, 2001, 2003), Moura and Steffen (2004), Peairs *et al*. (2004), Moura and Steffen (2006) and Palomino and Steffen (2009). This is an experimental technique and it is based on the piezoelectric effect, which couples the mechanical and the electrical domains.

In most applications of the ISHM, a piezoelectric transducer (PZT) is employed to interact with the monitored structure. The transducer must be bonded or embedded to the target structure and an electrical excitation will return information about the so-called "state of health" of the structure. Several types of pre/post-processing of the collected data can be employed to better evaluate the target structure. The next section describes the EMI technique in detail.

1.1. Physical principle of the EMI technique.

The EMI technique is considered to be a non-destructive method for evaluating different types of structures (NDE), as stated by Park G., *et al* [2003]. The only modification required is to bond the PZT to the target structure or to embed it (in the case a new structure is in the process of fabrication. In any case, since the transducer is very small and thin (thickness less than 1mm and less than 20mm in diameter for a disc patch), there are no major problems in incorporating these transducers into the target structure. Figure 1 presents a set of ceramic PZT, made of lead-zirconate-titanate (PZT) and produced by *MPI Ultrasonics,* and Figure 2 illustrates an aircraft aluminum window panel instrumented with six PZT patches.

Figure 1: Examples of ceramic PZT transducers. Source: www.mpi-ultrasonics.com).

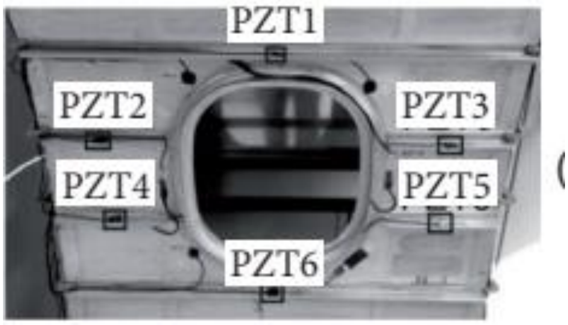

Figure 2: Aircraft aluminum window panel instrumented with six PZT patches (source: Maruo *et al*, 2015)

Independent of the shape, or even the material which the transducer is made of, the piezoelectric effect is what enables the electronic instrumentation of the target structure. This effect correlates the mechanical deformation of the transducer with a voltage at its terminals. It is possible to deform the transducer and obtain a differential voltage (direct effect) or to apply voltage and obtain mechanical deformation (converse effect). Figure 3 illustrates the direct and converse piezoelectric effects.

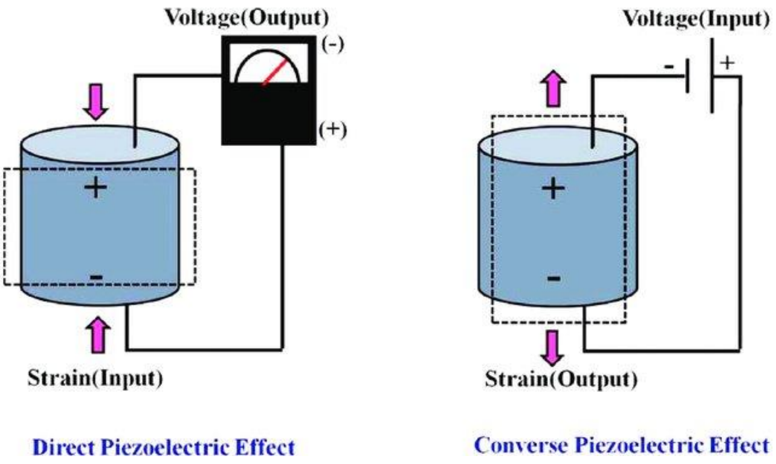

Figure 3: Direct and inverse piezoelectric effects. Source: Lakshmi *et al*, 2018.

In most cases, the PZT is fabricated to be sensitive to mechanical deformations applied to only one arbitrary direction, which can be perpendicular to the plane of bonding (or embedding) of the target structure. If the thickness of the bonding layer is considered to be not relevant, a simplified one degree of freedom (DOF) model may represent the bonded/embedded transducer. Figure 4 illustrates this 1 DOF model. The model reduces the complexity of the structure to a system represented by its mass, stiffness, and dampening. Any structural modification, like damage, will change at least one of those properties.

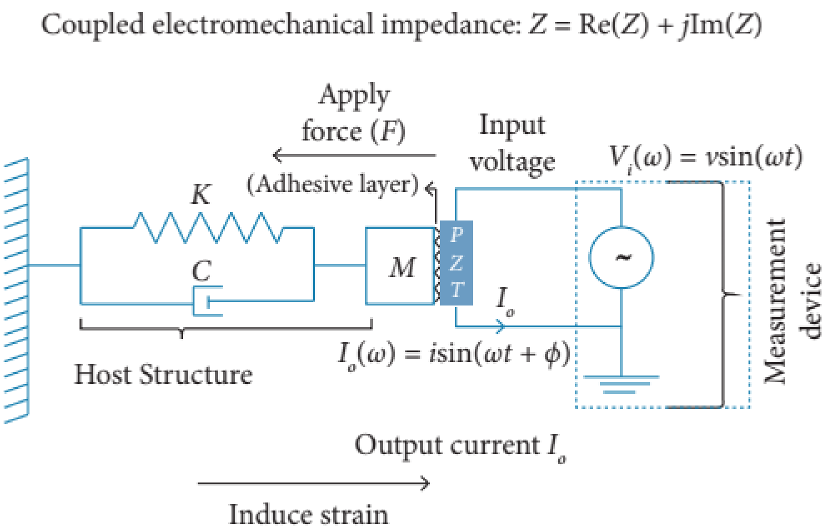

Figure 4: Mechatronic 1 DOF model of the coupled electromechanical transducer (source Maruo *et al* (2015)).

A sinusoidal voltage, with an arbitrary high-frequency band (tens to hundreds of kHz) and low amplitude (1V to 10V), is applied to the transducer. An equivalent strain will be applied to the coupled structure and the total circulating electrical current will be related to the transducer's electrical impedance and, also, the so-called **mechanical impedance** of the structure.

The **mechanical impedance** can be defined as a measure of how much a structure resists motion when subjected to a harmonic force. This property is also highly tied to other mechanical properties like mass, stiffness, and damping. In this case, the harmonic force is provided by the piezoelectric transducer (converse effect). So, the deformation of the bonded transducer will be directly affected by the mechanical impedance of the structure. The conclusion is that de equivalent impedance of the PZT will also be directly affected by the mechanical impedance. Liang *et al (*1994) modeled the so-called **electromechanical impedance** (EMI) of the coupled transducer as a function of frequency, as presented in equation (01).

$$Z_E(\omega) = \frac{V_i(\omega)}{I_O(\omega)} = \frac{h_a}{j\omega w_a l_a}\left[\bar{\varepsilon}_{33}^{T}(1-j\delta) - \frac{Z_S(\omega)}{Z_S(\omega)+Z_a(\omega)} d_{3x}^2 \bar{Y}_{22}^{E}(1+j\eta)\right]^{-1} \quad (01)$$

Where:

- $Z_E(\omega)$ represents the electrical admittance (inverse of electrical impedance); ω is the excitation frequency;
- $\bar{Y}_{11}^2$ is the complex Young's modulus of the PZT at zero electric field;
- d_{3x}^2 is the piezoelectric strain constant in the arbitrary x-direction at zero stress;
- ε_{33}^T is the dielectric constant at zero stress; and a is a geometric constant of the PZT;
- is the dielectric loss tangent of the piezoelectric patch;
- $Z_s(W)$ represents the mechanical impedance of the monitored structure and any structural changes will represent new values for $Z_S(\omega)$ and, consequently, for $Z_E(\omega)$.

Usually, the frequency of the sinusoidal voltage applied to the PZT is between 20kHz and 1MHz, where the upper limit is defined by the impedance analyzer and the electrical characteristics of the PZT employed.

Measuring the impedance over a frequency band will return a waveform (impedance versus frequency) that can be used to identify the mechanical state of the target structure at the moment of that measuring. The next section will describe the way to evaluate those frequency-dependent waveforms to characterize de "state of health" of the target structure.

1.2. Impedance signatures and Damage indexes.

If external effects like temperature variations and static or dynamic loads, on the monitored structure, were not taken into account, an Impedance Signature (IS) is a bi-dimensional waveform that describes the structure's EMI over an arbitrary and limited frequency band. Instruments like the impedance analyzer HP4194A are employed to obtain de IS from any kind of PZT patch. The HP4194A can obtain an IS with 400 frequency points and with an upper frequency bound of 1GHz.

The definition of the lower and the upper bounds of the frequency band depends on the complexity of the structure and the characteristics of the damage that is subject to identification. This statement may appear very nebulous and imprecise but authors like Chaudhry *et al* (1995, 1996), Palomino *et al.* (2011), Finzi Neto *et al.* (2010), Liang *et al.*

(1994), Moura *et al.* (2004) Park *et al.* (1999, 2000, 2001, 2003), Sun *et al.* (1995) and many other confirm it. In reality, for large and complex structures, the frequency band may be defined through experimental testing. But there are a few indicators on how to proceed. Small damages, like cracks, can be better identified at higher frequencies (hundreds of kHz), and higher the frequency shorter the range of sensing of the PZT, Rabelo, *et al.* (2017).

As an example, consider the experiment proposed by Bitencourt and Steffen Jr. (2009) with the aluminum beam illustrated in Figure 5. There are two ceramic PZT patches, PZT_1 and PZT_2, bonded to that beam and a rivet inserted on the right side. The removal of the rivet was used to simulate damage on the beam. Besides the damage, this example also illustrates the attempt to "repair" the beam with the insertion of another rivet at the same position. Each PZT patch had there IS measured over arbitrary and different frequency bands. The experimental procedure is described as follows:

(1) – Measure the IS, of each PZT, with no change on the instrumented structure [BASELINE];
(2) – Remove de rivet and measure the IS of each PZT again [STATE1];
(3) – Insert a new rivet in the same position that it was removed.
(4) – Measure the IS of each PZT for the last time. [STATE 2].

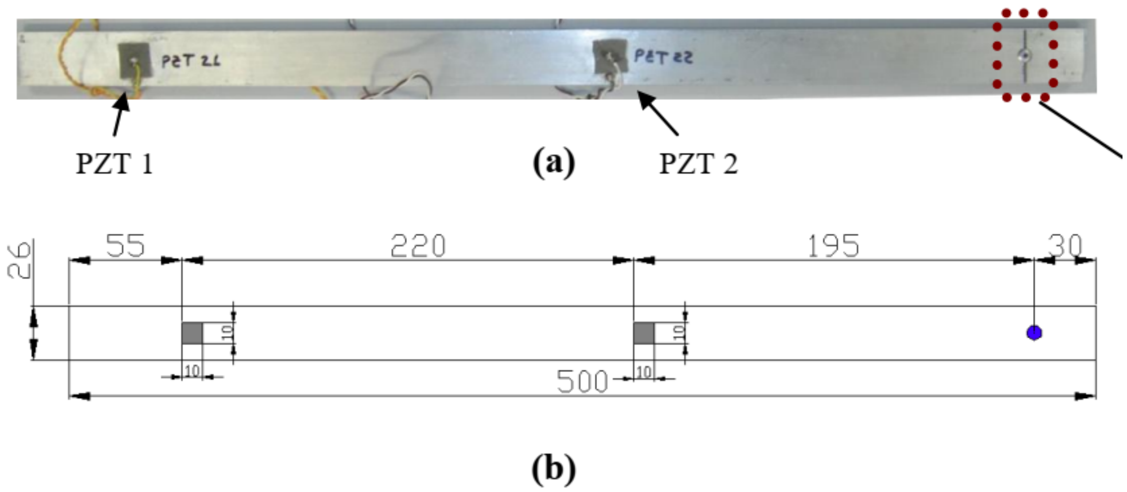

Figure 5: Aluminum beam (a) with ceramic PZT patches and a rivet used to simulate damage by its removal. The dimensions are presented at (b). Source: Bitencourt and Steffen Jr. (2009).

The collected IS for this experiment are presented in Figure 6. But, before trying to interpret the IS for the 3 states together, it is important to understand the IS by itself. The **characteristics of the quality** of an IS are presented as follows:

I. From Equation 01, it is well known that the EMI is a complex quantity (real part plus imaginary part). The imaginary part includes the reactive capacitance of the PZT and it is very influenced by temperature changes. So, to mitigate this effect, the IS are limited to only the real part of Z_E.
"Good" IS are the ones that present high and steep transitions in their values over their frequency range. This can be understood as a "reasonable" number of peaks and vales on the IS.

II. The defined frequency band should be related to the kind of damage/changes that are expected to happen on the target structure. Determining the frequency range, for a complex structure requires a set of experiments to better understand the EMI structure's behavior over the frequency. Nevertheless, studies are using mathematical models to help define the frequency range, Bhalla S., Soh (2004).

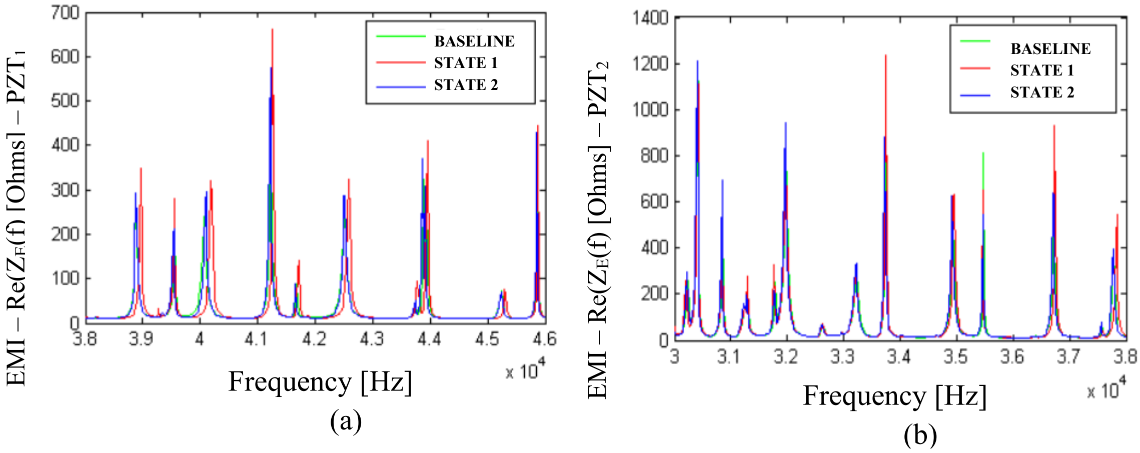

Figure 6: IS for PZT1 (a) and PZT2 (b) considering the three states [BASELINE, STATE 1, AND STATE 2]. Source: Bitencourt and Steffen Jr. (2009).

Taking into account those **characteristics of quality,** the following preliminary analysis can be done:

- All collected IS from Figure 6 are in accordance with (I) and (II). A "good" IS and only the real part of Z_E is considered;
- The differences in each of the three states, for PZT_1, can be clearly visualized. For PZT_2, this difference is more difficult to see.
- Even though a new rivet is inserted to replace that on it was removed, neither PZT presented an IS (for STATE 3) that was visually identical to their respective BASELINE. It must be understood that even a so-called "identical repair" is employed on the target structure the correspondent IS will never be the same as before de damage [Chaudhry *et al* (1995, 1996), Finzi Neto *et al.* (2010), Liang *et al.* (1994), Moura *et al.* (2004) Park *et al.* (1999, 2000, 2001, 2003), Sun *et al.* (1995)];

From the preliminary analysis, it became clear that only the visual inspection of the collected IS, in each state, is not enough to quantify the structural modifications (damage) on the aluminum beam.

A better way to analyze the IS is to mathematically quantify the difference between each state into a single number. A **damage index** is a mathematical way to quantify the difference between two IS obtained from the same bonded PZT. Palomino and Steffen Jr (2009) have evaluated several damage indexes for simulated damage on an aircraft aluminum panel. From those, the most commonly used ones are described as follows.

For every damage index described here, consider these definitions:

- $Re(Z_{1,i})$ is the array of impedance (resistance) points measured under "healthy conditions" (baseline);
- $Re(Z_{2,i})$ is the array of the real part impedance points measured in any other mechanical state than the baseline;
- $Re(\bar{Z}_1)$ mean value of the real part impedance points measured under "healthy conditions" (baseline);
- $Re(\bar{Z}_2)$ mean value of the real part impedance points measured in any other mechanical state than the baseline;
- $S_{Z_{1},i}$ for a set of *k* IS collected at the baseline state, this is an array of standard deviation values, calculated with the *k* values, at each of the *n* array indexes;
- *n* is the number of impedance points.

RMSD – Root Mean Square Deviation.

$$RMSD = \sqrt{\sum_{i=1}^{n}\left(\frac{\left(Re(Z_{1,i}) - Re(Z_{2,i})\right)^2}{n}\right)} \tag{02}$$

This is the most common damage index in the scientific literature. The RMSD number will always be positive and its magnitude shall not be influenced by the number of impedance points in the IS.

RMSD1 – Root Mean Square Deviation (alternative 1).

This is the first variant of the RMSD. Grisso (2005) has presented the RMSD1 as an alternative that is less sensitive to the amplitude of the impedance's amplitude. This variant, equation (03), presented good results on quantifying damages associated with variation in quantity and location of the impedance peaks and valleys in the IS for each state.

$$RMSD1 = \sqrt{\sum_{i=1}^{n}\left(\frac{\left(Re(Z_{1,i}) - Re(Z_{2,i})\right)^2}{Re(Z_{1,i})^2}\right)} \tag{03}$$

RMSD2 – Root Mean Square Deviation (alternative 2).

The damage index presented in equation (04) has been used in a few studies comparing the sensibility of damage detection, Tseng *et al* (2002) and Giurgiutiu *et al* (2005). It presents a slightly different mathematical definition from the RMSD1.

$$RMSD2 = \sqrt{\frac{\sum_{i=1}^{n}\left(Re(Z_{1,i}) - Re(Z_{2,i})\right)^2}{\sum_{i=1}^{n} Re(Z_{1,i})^2}} \tag{04}$$

RMSD3 – Root Mean Square Deviation (alternative 3).

Park *et al* provided another alternative for the original RMSD. In equation (05), the sum is outside the root mean square sign, unlike the definitions previously given. The authors claim that this version of the RMSD is more robust and less sensitive to impedance peaks variations.

$$RMSD3 = \sum_{i=1}^{n} \sqrt{\frac{\left(Re(Z_{1,i}) - Re(Z_{2,i})\right)^2}{Re(Z_{1,i})^2}} \tag{05}$$

RMSD4 – Root Mean Square Deviation (alternative 4).

This alternative includes the mean values of each IS analyzed. The authors claim that equation (06) is less sensitive to external effects, like temperature variations, that result in different kinds of variations in the IS.

$$RMSD4 = \sqrt{\sum_{i=1}^{n} \left(\frac{\left(\left(Re(Z_{1,i}) - Re(\bar{Z}_1)\right) - \left(Re(Z_{2,i}) - Re(\bar{Z}_2)\right)\right)^2}{n} \right)} \tag{06}$$

RMSD5 – Root Mean Square Deviation (alternative 5).

External effects, like temperature variations, are always present in industrial applications and must be mitigated with specific techniques that will be later described in this chapter. Meanwhile, the RMSD5 tries to mitigate this problem with a set of *k* IS collected at each state of interest (baseline, state1, …). Those differences, due to the external effects, will be mitigated in the damage index value.

$$RMSD5 = \sqrt{\sum_{i=1}^{n} \left(\frac{\left(\frac{Re(\bar{Z}_{1,i}) - Re(Z_{2,i})}{S_{Z_{1},i}} \right)^2}{n} \right)} \tag{07}$$

CCD – Correlation Coefficient Deviation.

A more statistical approach is presented by the CCD damage index described by Giurgiutiu (2014). It measures the linear relationship between two IS from different states and it is defined in equation (08).

$$CCD = 1 - \frac{\sum_{i=1}^{n}\left(Re(Z_{1,i}) - Re(\bar{Z}_1)\right)\left(Re(Z_{2,i}) - Re(\bar{Z}_2)\right)}{\sqrt{\sum_{i=1}^{n}\left(Re(Z_{1,i}) - Re(\bar{Z}_1)\right)^2 \sum_{i=1}^{n}\left(Re(Z_{2,i}) - Re(\bar{Z}_2)\right)^2}} \tag{08}$$

The main advantage of this damage index is that its values are always normalized, which could be helpful to verify the progression of the damage in some types of structures.

There are many others damage indexes (MAPD, ASD, M, etc.) but they are less present in the literature than those aforementioned in equations (02) to (08), Palomino (2009).

Returning to the evaluation of the IS presented in Figure 06, the RMSD damage index was used to quantify the difference between a baseline IS and the IS for STATE 1 and STATE 2, for each PZT. The following bar graphs illustrate the results.

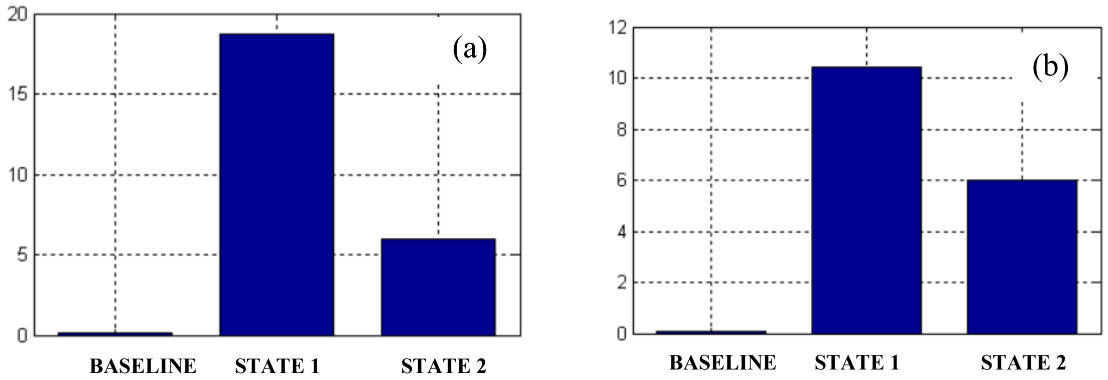

Figure 7: RMSD damage indexes for PZT1 (a) and PZT2 (b), considering the three states [BASELINE, STATE 1, AND STATE 2]. Source: Bitencourt and Steffen Jr. (2009).

What is most interesting, from the results illustrated in Figure 7, is that the RMSD values from PZT2 are lower than the ones from PZT1. Since PZT2 is nearer the location of the removed bolt (STATE 1), one would expect that those RMSD values should be higher for this PZT. Nevertheless, the difference in the band frequency applied to each PZT can help to explain these results. Another set of factors that can describe these results are the thickness of glue bonding each PZT and differences in PZT polarization due to the fabrication process.

In laboratory experiments, it is most common to use specialized equipment, like the expensive and bulky impedance analyzer HP4194A. This instrument can analyze only one connected PZT at a time but provides a rich set of information about the PZT's impedance. Industrial applications it is required a less costly solution that is capable of using many PZT transducers at the same time. The next section describes how the PZT´s impedance can be measured to build low-cost circuits capable of operating dozens of PZTs.

1.3. Modeling the electrical portion of the EMI.

Only the electrical portion of the EMI can be directly measured using conventional or more specialized instrumentation systems. It expresses a complex valued function dependent on the excitation frequency. For each corresponding frequency, the electrical part of the EMI can be represented in terms of the real and imaginary parts, or magnitude and phase in its polar form. Defining the sinusoidal excitation $v(\omega, t)$, with angular frequency $\omega = 2\pi f$, Figure 08(a) describes a PZT impedance as a simple resistor-capacitor circuit. In Figure 08(b) the waveforms of voltage and current are illustrated.

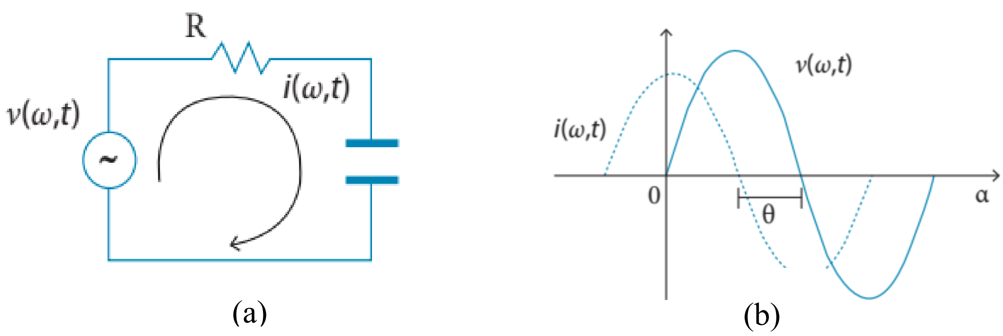

Figure 8: EMI equivalent circuit under sinusoidal excitation (a) and the waveforms of $v(\omega, t)$ and $i(\omega, t)$. Source: Maruo *et al* (2015).

Knowing that the more specialized impedance analyzers continually optimize the voltage amplitude applied to a DUT (Device Under Test) and amplitude of the resulting current is dependent on the EMI, equations (09) and (10) mathematically describe those waveforms.

$$v(\omega,t) = V(\omega)\, sin(\omega t) \tag{09}$$

$$i(\omega,t) = I(\omega)\, sin(\omega t + \theta) \tag{10}$$

Applying the well-known Ohm´s Law, the $Z_{EMI}(\omega)$ can be calculated measuring $i(\omega,t)$ and θ. Equations (11), (12) and (13) calculate the EMI and its complex/polar decomposition.

$$Z_{EMI}(\omega) = \frac{v(\omega,t)}{i(\omega,t)} = \frac{\mathcal{F}(v(\omega,t))}{\mathcal{F}(i(\omega,t))} = \frac{V(\omega)}{I(\omega)} = R(\omega) - iX_C(\omega) = |Z_{EMI}(\omega)|\angle\theta \tag{11}$$

$$Re(Z_{EMI}(\omega),\theta) = Z_{EMI}(\omega)\cos(\theta) = R(\omega) \tag{12}$$

$$Im(Z_{EMI}(\omega),\theta) = Z_{EMI}(\omega)\sin(\theta) = X_c(\omega) \tag{13}$$

For ISHM applications, it has already been stated that the resistive part of the EMI, equation (12), is more stable when temperature variations are taken into account. Nevertheless, there are cases where the reactive part of the EMI, equation (13), brings information about the PZT bonding, Grisso and Inman (2009).

1.4. The EMI measurement problem.

If you can use the impedance analyzer HP4194A your only problem is the space required to accommodate that bulky machine. Nevertheless, for industrial application, a less costly, smaller, and the lighter solution must be employed.

Through the years, the literature has presented different types of instrumentation systems capable of measuring and digitalizing the electrical impedance of a bonded PZT transducer, Finzi Neto *et al* (2011) and Baptista *et al* (2009). But, in all of them, the problem remains on measuring $i(\omega,t)$ and θ.

Measuring $i(\omega,t)$ is really simple and uses a well-known analog electronic circuit based on an operational amplifier. The electronic circuit illustrated in Figure 9 is a low-cost and simple solution. Using a precise and low value shunt resistor ($R_{shunt} \approx 100\Omega$), $i(\omega,t)$ can be calculated from $Vr(\omega,t)$ after being acquired by a data acquisition card (DAq).

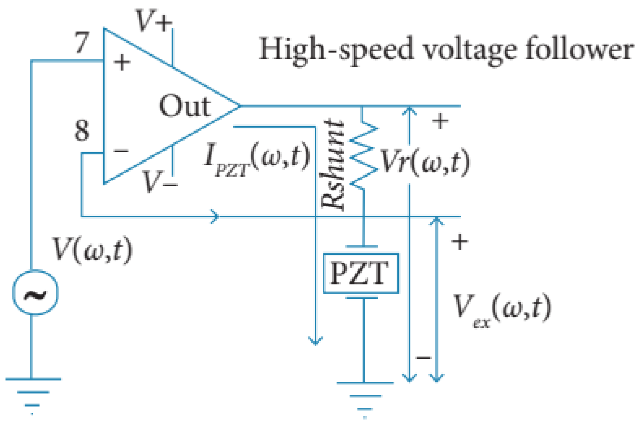

Figure 9: Electronic circuit used to measure $i(\omega,t)$. Source Maruo *et al* (2015).

From figure 9, *V(ω,t)* is any sinusoidal voltage source that can vary its frequency over an arbitrary frequency band. In most cases, the same DAq used to acquire *Vr(ω,t)* can generate *V(ω,t)*, Baptista (2009).

After acquiring *V(ω,t)* and *Vr(ω,t)*, it is required to transpose both of them to the frequency domain. A Fast Fourier Transform (FFT) can be easily applied to *V(ω,t)* and *Vr(ω,t)*, allowing for the use of equations (11) and (12) to calculate *R(ω)*.

Even though a DAq associated with one or more analogic circuits is less costly than the HP4194A, the ISHM will always be limited to the data acquisition rate of that card. There is some controversy about the use of the Nyquist Theorem as the time-domain requisite to process a time-domain signal in the frequency domain, Finzi Neto (2010) and Baptista (2009). The problem that arises is related to how accurate is θ, from equations (11) and (12), calculated near the upper limit of the Nyquist's frequency signal. Experimental results presented and discussed on the works of Finzi Neto *et al* (2010), Maruo *et al* (2015), Martins *et al* (2013) and Tsuruta *et al* (2017) shows and or discuss the deterioration of *R(ω)* near the upper limit of the signal's data acquisition frequency. Of course, there are plausible arguments that the so-called deterioration of *R(ω)* is neglectable, Baptista (2011).

There are other architectures of electronic circuits where DAq's acquisition frequency and FFTs are no longer a limiting factor for ISHM applications. Maruo *et al* (2015) propose an architecture based on the digital signal controller (DSC) and specialized circuits for analog frequency processing. Beyond that, their architecture can monitor a large number of PZTs using analog multiplexed electronics. Figure 10 illustrates the proposed hardware.

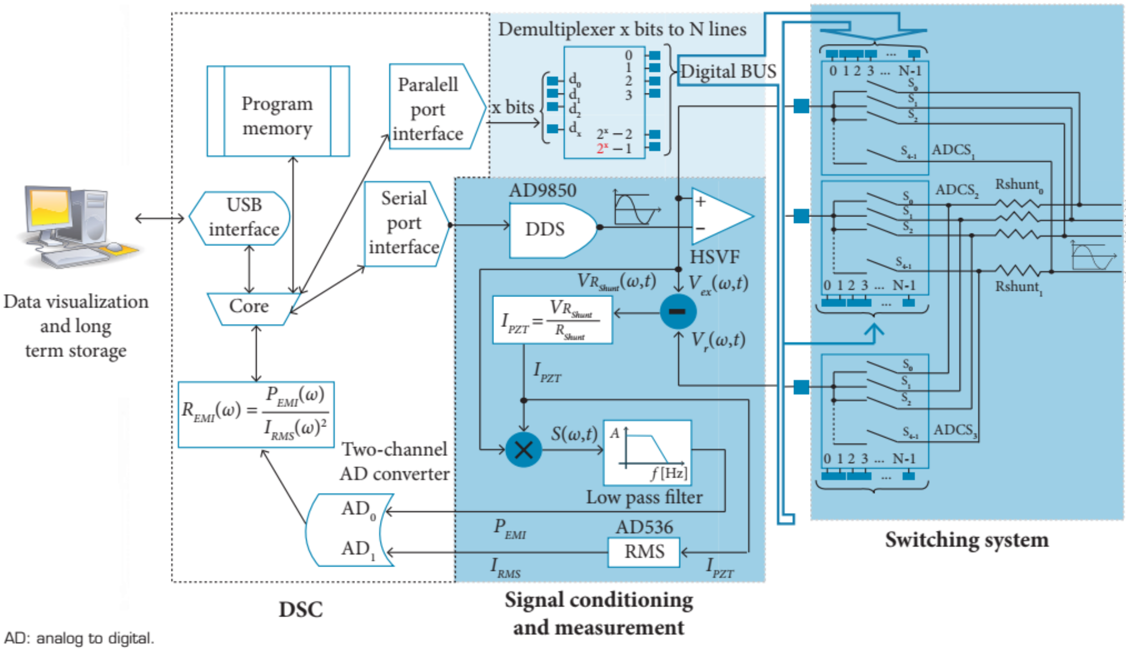

Figure 10: Architecture of a multiplexed sensor array for ISHM applications. Source: Maruo *et al* (2015).

No DAq is employed to acquire *Vr(ω,t)* and or to generate *V(ω,t)*. The sinusoidal signal is generated by an integrated circuit, the AD9850, which is digitally programmed by the DSC. To avoid the use of temporal signals, the authors employed the dedicated integrated circuit AD536, from Analog Devices, to generate voltages proportional to the Root Mean Square (RMS) value of each sinusoidal waveform. To be able to calculate *R(ω)*, the author proposes to analogically calculate the mean power drained by the PZT using the proposed topology in Figure 11. The dedicated integrated circuit, AD633, multiply *Vr(ω,t)* and *i(ω,t)* to produce an analog waveform representing the apparent power, *S(ω,t)* consumed by the PZT. A Second-Order Low Pass Filter (SOLPF) is used to separate the mean power *P(ω)*.

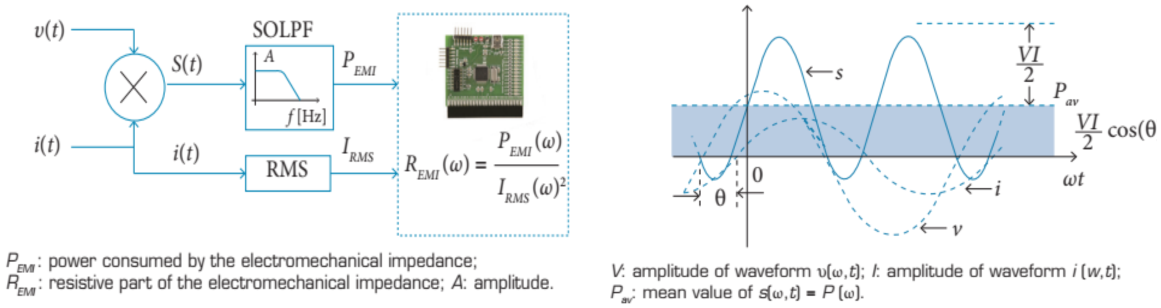

Figure 11: Topology to obtain the mean power $P(\omega)$ (a). Equivalent waveforms (b). Source: Maruo *et al* (2015).

Finally, the authors state that $R(\omega)$ is easily calculated from equation (14).

$$R_\omega = \frac{P_\omega}{I_{RMS}(\omega)^2} \tag{14}$$

Since $P(\omega)$ and $I_{RMS}(\omega)$ ideally have little to no alternating component, the authors states that an acquisition frequency as low as 1000 samples per second may be used to rapidly acquire PZT responses. The only operational limitation is related to the frequency band response of the integrated circuits AD633, AD536 and AD9850.

There are lots of other so-called low-cost topologies for the IEM measurement problem. It is up to the reader to choose the one that best suits the intended industrial application.

After collecting the IS for each state (baseline, state 1, …) it is important to pre-process each IS to identify and separate the influences of external effects, like temperature variations and static loading, from the real information in each IS. The next section will describe how these effects modify the IS and a few ways to mitigate this problem.

1.5. Influence of external effects on the IS.

When a new monitoring system is proposed it is necessary to evaluate the possibility of external influences deteriorating the signals collected from the transducers. External influences like temperature variations (TR), magnetic interference (MI), electromagnetic interferences (EMI), radio frequency interferences (RFI), mechanical static loads (MSL), mechanical dynamic loads (MDL), and an ionic environment (IEnv) may contaminate the electrical signal provided by the transducer or may alter the mechanical properties of the monitored structure. In any case, there are several ways to mitigate every external effect that is mentioned here.

Palomino *et al* (2012) examined the influence of electromagnetic radiation, temperature and pressure variations, and the ionic environment under laboratory conditions. In this context, the major concern was to determine if the impedance responses are affected by these influences. In addition, the sensitivity of the method concerning the shape of the PZT patches was also evaluated. For this aim, two shapes of piezoelectric patches of the same size, namely circular and squared, have been tested in the laboratory. They were bonded to two different types of structures, namely a plate and a beam so that the impedance response was measured both for pristine and damaged conditions. Similar results were obtained for the two shapes of PZT patches tested. The results are summarized in Table 1, in which it can be observed that temperature is a major environmental issue in the context of ISHM.

Table 1 – Sensor shape and environmental influences. Source: Palomino *et al* (2012).

Sensor Geometry		Ionic Environment	
Squared PZT Patch	Circular PZT Patch	Without shielded PZT patch	With shielded PZT patch
 =		 YES	 NO
Electromagnetic Radiation	Temperature		Pressure
	Low	High	
 NO	 NO	 YES	 NO

The temperature influence brings the most undesirable effect for industrial applications: **false positives** of damage detection**.** Under temperature variations changes in the stiffness and dampening, on the monitored structure, will be presented on the IS. Therefore, IS collected in different temperatures will be so different that any damage index would indicate severe damage on the monitored structure.

Before devising ways to mitigate the temperature effect problem, it is important to understand how the IS is altered due to those temperature variations. Consider the experiment performed by Rabelo *et al* (2017b). The authors have bonded a PZT in the center of an aluminum 2024-T3 plate measuring 305mmx305mmx2mm and used an environmental controlled chamber, ESPEC EPL-4H, to control the temperature, Figure 12(a). The authors varied the temperature inside the chamber from 0°C to 50°C, in steps of 10°C. At each temperature step, an IS was collected. All the IS, at each temperature step, are presented in Figure 12(b).

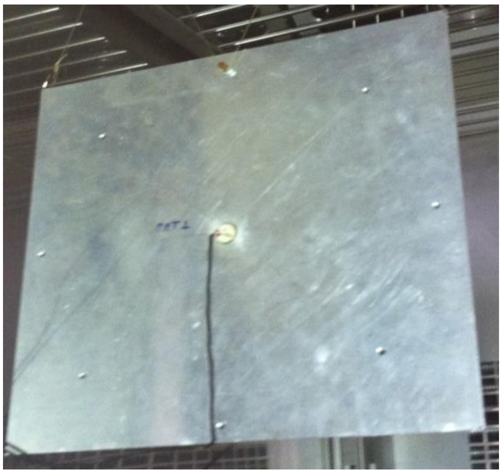

(a)

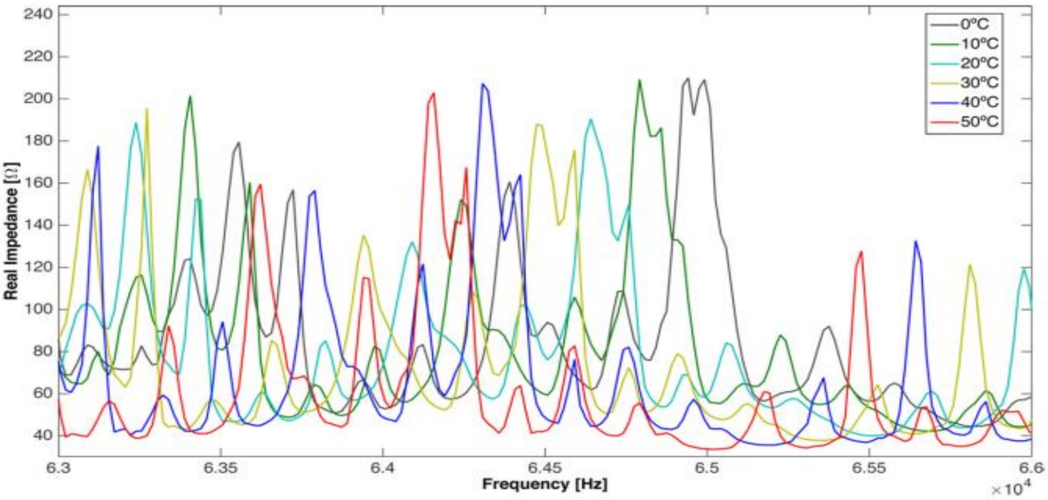

(b)

Figure 12: Temperature variation effects on impedance signatures: (a) instrumented Aluminium plate of 305 mm x 305mm x 3mm and (b) impedance signals shifted with temperature changes. Source: Rabelo (2017b)

The authors stated that the frequency band, 63kH to 66kHz, as defined by trial and error, looked for the already mentioned **characteristics of quality**. By analyzing Figure 12(b), the effects of temperature can be observed predominantly as horizontal shifts due to changes in the resonance frequencies of the system. Vertical shifts can also be seen, as well as changes in some peak amplitudes. The more temperatures get higher, the more shift horizontally to the left and vertically down can be seen. Analogous thinking can be done when temperatures get lower.

There are several ways to mitigate the temperature effect on the IS. Rabelo *et al* proposed a method based on horizontal frequency shifts to mitigate the most predominant effect of temperature variations. Figure 13 presents the compensated IS. Although the horizontal shifts were compensated, differences in peak values are still visible. These differences will limit the sensibility of the IEM method and the so-called **statistical threshold of detection** is proposed by the authors.

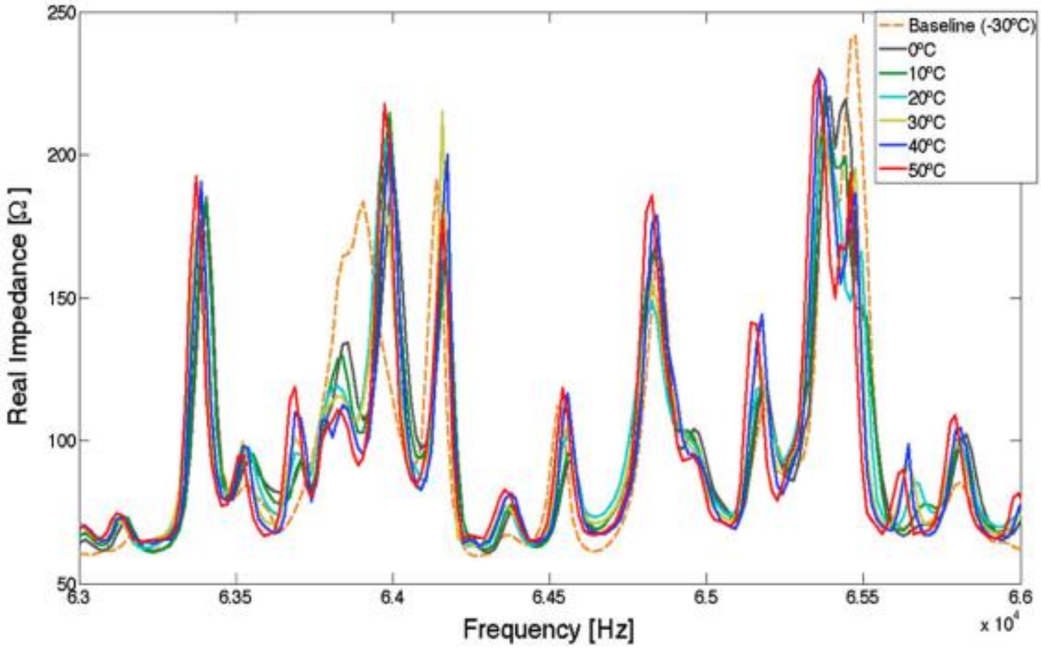

Figure 13: Impedance Signatures, from Figure 12, after the temperature compensation algorithm was applied. Source: Rabelo *et al* (2017b).

The fundaments behind the statistical process control allow for establishing limits in a control chart so that a threshold can be established using the upper control limit. These limits can be defined so that 95.45 or 99.73% of data from a normally distributed population remains if these control limits are established as expressed in equation (15), where x is the sample mean and s is the sample standard deviation.

$$\begin{aligned} \bar{x} \pm 2s - \ for\ 95{,}45\%\ of\ confidence \\ \bar{x} \pm 3s\ - for\ 99{,}73\%\ of\ confidence \end{aligned} \tag{15}$$

From equation (15), it is the upper limit that must be considered to identify the so-called **threshold of damage detection** with a certain level of confidence. The authors continue to the argument that the sampled mean and sampled standard deviation are inferences from the population parameters (i.e., unknown values). Therefore, a more robust methodology should be proposed by using the upper limits of the confidence intervals for the population mean and standard deviation according to equations. (16) and (17), respectively.

$$\left[\bar{x} - \frac{st_{v;\alpha/2}}{\sqrt{N}} \leq \mu_x \leq \bar{x} + \frac{st_{v;\alpha/2}}{\sqrt{N}}\right] v = N - 1 \tag{16}$$

$$\left[\frac{vs^2}{x^2_{v;\alpha/2}} \leq \sigma_x^2 \leq \frac{vs^2}{x^2_{v;1-\alpha/2}} v = N - 1\right] \tag{17}$$

where N is the sample size, μ_x and σ_x^2 are the population mean and variance, respectively, x and s^2 are the sample mean and variance, respectively, $t_{v;\alpha/2}$ has a *Student t* distribution with v degrees of freedom, α is the significance level and $x^2_{v;\alpha/2}$ has a Chi-Square distribution.

Hence, the upper limit of the confidence intervals was used and the threshold for each PZT transducer was determined according to equation (18).

$$PZT_{threashold} = \mu_{x\,max} + 3\sigma_{x\,max} \tag{18}$$

Where $\mu_{x\,max}$ is the upper limit for the population mean and $\sigma_{x\,max}$ is the upper limit for the population standard deviation, both obtained by choosing 5% of significance level α.

In practical terms, equation (18) will be applied to the damage indexes calculated for each temperature compensated IS, at the central temperature. Those sets of calculated damage indexes will have a mean value $\mu_{x\,max}$ a standard deviation of $\sigma_{x\,max}$. The threshold, a starting damage index value at which damage has the confidence of 99,73%, will be calculated with equation (18). Rabelo *et al* (2017b) present a set of experiments to prove the efficiency of the temperature effect compensation method and the threshold calculation. A more in-depth analysis may be found in their paper.

1.6. Final remarks

ISHM has been used in different industries over the years. The aircraft industry has been the pioneer. In Brazil, EMBRAER and many federal Universities have been developing new hardware and processing techniques for real-time and in-service applications.

The civil construction industries are following the same steps. Research works like the one developed by Silva, R.N *et al* (2020) are proving that ISHM is a low-cost alternative for monitoring aging and in-service concrete-based structures.

Several new alternatives have emerged to deal with the temperature compensation problem. Freitas et al (2021) propose a neuro-fuzzy model and Ferreira de Rezende et al (2020) propose a deep learning approach with convolutional neural networks. In this last approach, it is proposed that the temperature compensation in the pre-processing is not carried out like the other approaches. Thus, the identification and classification model must be able to understand different types of signatures as a baseline, as well as different possibilities for the same damage signature.

Effects like dynamic loading are not a factor to disregard ISHM, anymore. Research works like the ones developed by Rabelo *et al* (2017a and 2017b) and Cavalini, A. A. *et al* (2014) proved that there are efficient ways to mitigate these influences for in-service structure monitoring.

Finally, as an indication for future and innovative applications, Menegaz *et al* (2019) studied the application of ISHM in the detection of mammary inclusions (tumors). Furthermore, some mathematical-statistical approaches have emerged to complement the damage location capability as described by Golçalves et al (2021) who use geostatistical kriging techniques associated with the ISHM.

There are lots of paths to follow with the research in ISHM. The industry will decide which ones will become final products. But it is up to the researchers to present these many alternatives.

1.7. Experimental Example

To illustrate the procedure of the Impedance-based SHM Methodology and its main aspects, an experimental test was proposed as follows.

In this experiment, the specimens used were four aluminum beam structures monitored inside a Platinous EPL-4H series climatic chamber for temperature and humidity control, as shown in Figure 14. This chamber is installed in the Structural Mechanics Laboratory (LMEst) of the School of Mechanical Engineering (FEMEC) at the Federal University of Uberlandia (UFU).

In this experiment, aluminum beams measuring 500 mm in length, 38 mm in width, and 3.2 mm in thickness were used. In each of them, a PZT patch measuring 1 mm thick and 20 mm in diameter was glued at 100 mm from the edge of the structure.

Figure 14: Platinous EPL-4H series climatic chamber used in this test.

First, after selecting the specimens, the PZT patches are bonded to each one. In this case study, epoxy glues with temperature tolerance up to 60-70 ^{o}C were used. Right after the patches were bonded to the structure, the measuring terminals were soldered. In this PZT patch type, it was necessary to use copper tape on the lower surface to make a better connection. This can be observed in Figure 15.

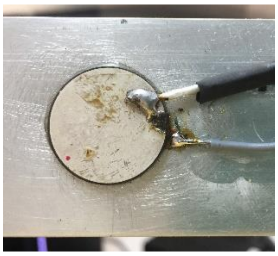

Figure 15: Specimen and PZT patch.

In this test, aluminum beams 500 mm in length, 38 mm in width, and 3.2 mm in thickness were used. In each of them, a PZT patch measuring 1 mm thick and 20 mm in diameter was bonded at 100 mm from the edge of the structure. Also, ABS plastic printing supports were designed to position the structures inside the chamber. Such structures have rounded bases to reduce the interference of the chamber floor with the structures and made it possible to adapt connectors to the samples. This type of connector embedded in the support structures allowed for less interference and noise addition to the cables during several removals of specimens from the chamber. Figure 16 illustrates one specimen, the support structure with the connector at the right end as well the PZT patch and damage position.

Figure 16: Specimen used in the test illustrating the PZT patch and damage position.

The simulated damage that was inserted into the structures was superficial and caused by grinding in a defined region. This machined region was 30mm wide at 70mm from the opposite end of the PZT patch. Thus, nine levels of damage were performed throughout the experiment, considering two reference levels and seven levels of gradual thickness removal. Throughout the experiment, only specimen 4 was kept without any changes for monitoring and controlling the process. However, specimen 4 was removed from the chamber together with the others at each machining process.

Figure 17 shows in better detail the connector attached to the structural support printed in ABS. This type of connector facilitates the process of removing and reinserting specimens for machining.

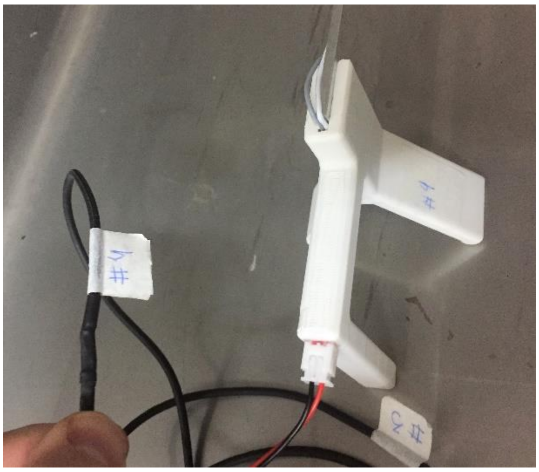

Figure 17: Specimen and connector.

In Figure 18, the test specimens are presented in the bi-supported condition. The support structures were designed to keep the specimens in this position because, during the thickness removal process, especially the terminal stages, the loss of structural stiffness could cause some kind of flexion at the two extreme support points.

Figure 18: All specimens used in the test.

Since the temperature has a significant impact on the impedance monitoring process, this factor was controlled in this case study through the climate chamber. Figure 19 illustrates the specimens positioned inside the chamber. It is important to note that the specimens must be positioned inside the chamber in such a way that the effects of convection flows (blowing) on some specimens are reduced, causing fluttering or measurement noise.

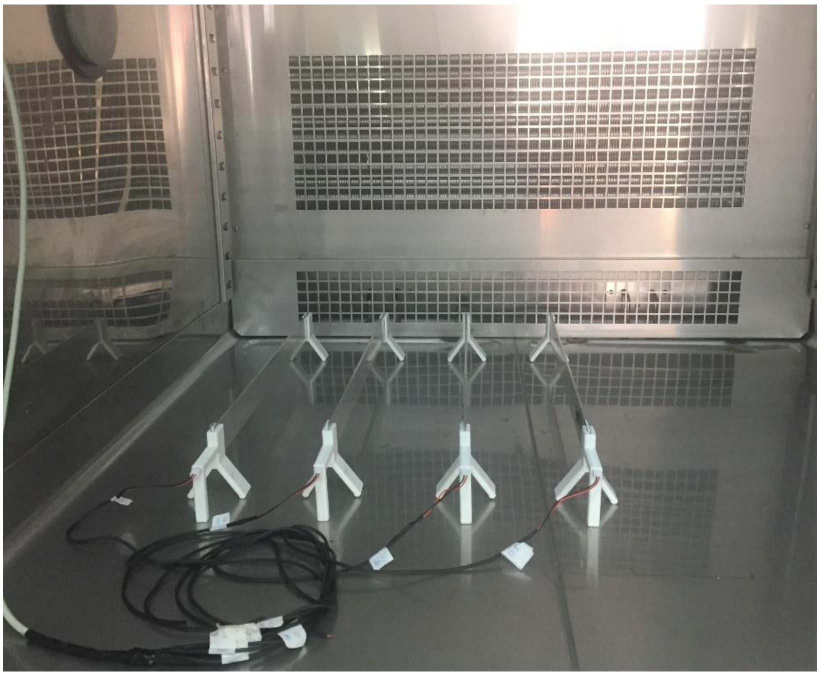

Figure 19: Specimens inside the chamber.

All specimens were monitored in ascending cycles of 3 ºC for a total of 11 temperature cycles. The impedance analyzer used for the acquisition and storage of signatures was connected externally to the chamber.

The temperature range used was from 10 to 40 ºC with levels of 3 ºC. As this level variation can be considered small for control and thermal stability purposes, a procedure was adopted. After the acquisition of each cycle of impedance signatures, the chamber increased its temperature by 3 ºC and remained for 30 minutes to stabilize the internal temperature and obtain the thermal balance between specimens and the environment.

For each configuration: specimen, temperature, and damage condition, 30 samples of impedance signatures were taken for process repeatability. Thus, in 11 temperature cycles, 9 damage levels, 4 specimens, and 30 repetitions, 11880 impedance signatures were acquired.

Considering that the process of reducing thicknesses by grinding is a manual task, two response variables of each specimen were selected for damage monitoring. The first response considered was the mass, considering the loss of mass about the previous state of integrity. In this case, a scale with two decimal places of the gram of precision was used. In addition, eight measurements were taken to obtain the average.

The second response variable was the thickness in the ground region, considering the loss of thickness from the previous condition. In this second answer, a micrometer with a resolution of 0.01mm was used and the average of 10 random measurements of thickness in the machined region was recorded. Figure 20 shows the ground region of one of the specimens during the thickness loss process.

Figure 20: Specimen and ground position.

Next, Tables 1 and 2 are presented, which correspond, respectively, to the response variables of the experiment, with the results of the measurements of mass and thickness for each specimen.

Table 1: Results of beam mass losses (in *g*).

Condition	Specimen #1	Specimen #2	Specimen #3	Specimen #4
Baseline	191.36	192.42	192.86	195.89
Damage #1	191.2	192.27	192.69	-
Damage #2	191.16	192.02	192.58	-
Damage #3	190.95	191.82	192.39	-
Damage #4	190.41	191.48	192.02	195.87
Damage #5	189.96	190.54	191.33	-
Damage #6	189.16	189.42	189.78	-
Damage #7	187.44	188.57	188.37	195.83

Table 2: Results of beam thickness losses (in *mm*).

Condition	Specimen #1	Specimen #2	Specimen #3	Specimen #4
Baseline	3.17	3.17	3.19	3.18
Damage #1	3.09	3.11	3.09	-
Damage #2	3.01	2.96	2.99	-
Damage #3	2.97	2.93	2.95	-
Damage #4	2.85	2.85	2.89	3.17
Damage #5	2.72	2.49	2.63	-
Damage #6	2.44	2.23	2.09	-
Damage #7	1.93	1.92	1.83	3.18

As can be seen in Table 2, the damage inserted in the three specimens did not exceed 50% of the thickness. Furthermore, the evolution between damage levels occurred more severely in the last two stages. This variation has a specific purpose of evaluating greater variations in damage models the greater the damage severities.

Another observation can be seen by comparing Tables 1 and 2 in specimen column #4. From this comparison, it can be said that based on the case study in question and on the measuring devices used, the measurement of thickness loss can be a more rigorous measurement criterion.

Considering the impedance-based structural integrity monitoring of the aluminum beams, Figure 21 presents the impedance signatures for specimen #1. Since this case study focuses on observing the basic principles of the technique, results are presented for this specimen only, but similar results were obtained for specimens #2 and #3. It is believed that repetitive presentation of other specimens would increase the volume of information unnecessarily to present the technique.

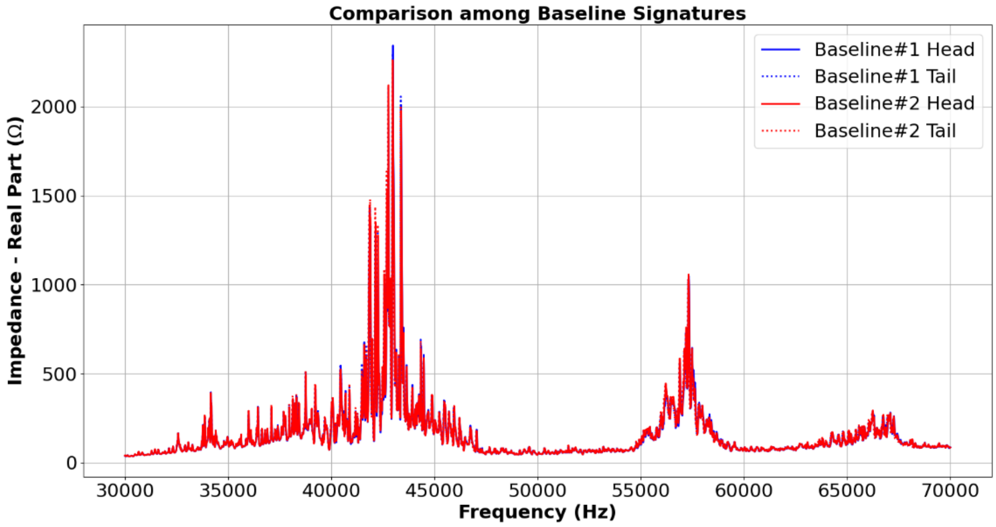

Figure 21: Specimen #1 and repetitive baseline signatures.

Figure 21 illustrates four impedance signatures from the experiment. There are presented the first and last impedance signature measured (head and tail) from the first temperature for the first and second group of baselines (Baseline #1 and #2). Explaining the objective of two sets of baseline measurements, a first group was measured, completing 30 repetitions for each of the 11 temperature levels, corresponding to 330 series. Then, all of the four beams were removed from the climate chamber, and it was transported along some buildings in the university to increase potential noise factors in a new measurement. Then, a few minutes later, the four structures were reinserted into the climate chamber and measured another set of baseline with 330 signatures.

According to Figure 21, it is possible to verify the repeatability of the signatures even with the potential insertion of small bending, small strains in the beams, and wired connections variations. This is one of the characteristics that make the use of the method applicable and reliable in real monitoring cases.

Figure 22, as described throughout the chapter, shows the temperature variation in the impedance signature under the same undamaged condition. The 11 temperature levels are not illustrated to facilitate an understanding of the phenomenon. However, the intermediate values between the ranges illustrated in the graph, present similar behavior.

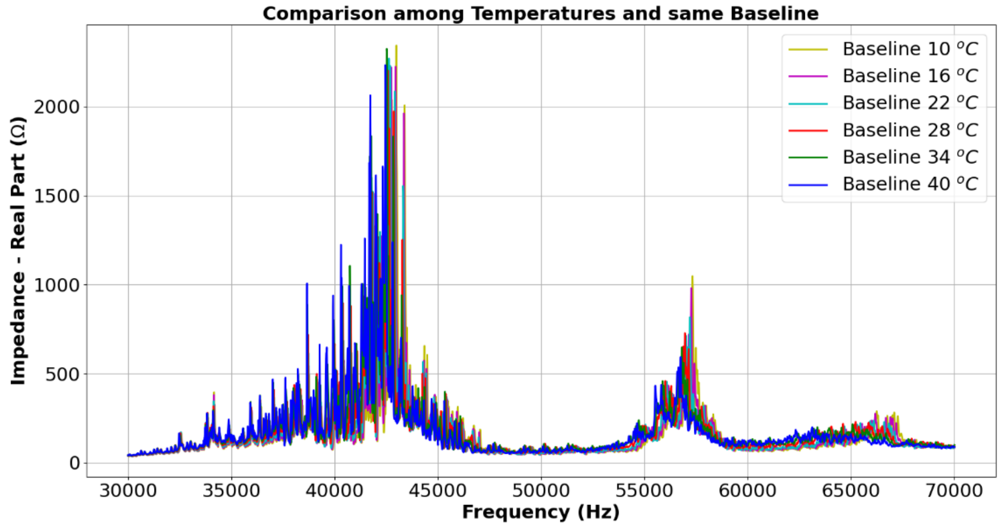

Figure 22: Specimen #1 and temperature changes for Baseline #1.

Since the frequency range in this experiment is wide, with 4000 sampling points, the effect of temperature in this figure may not be clear. In Figure 23, only the second region with the highest frequency peaks, around 54-60 kHz, is presented.

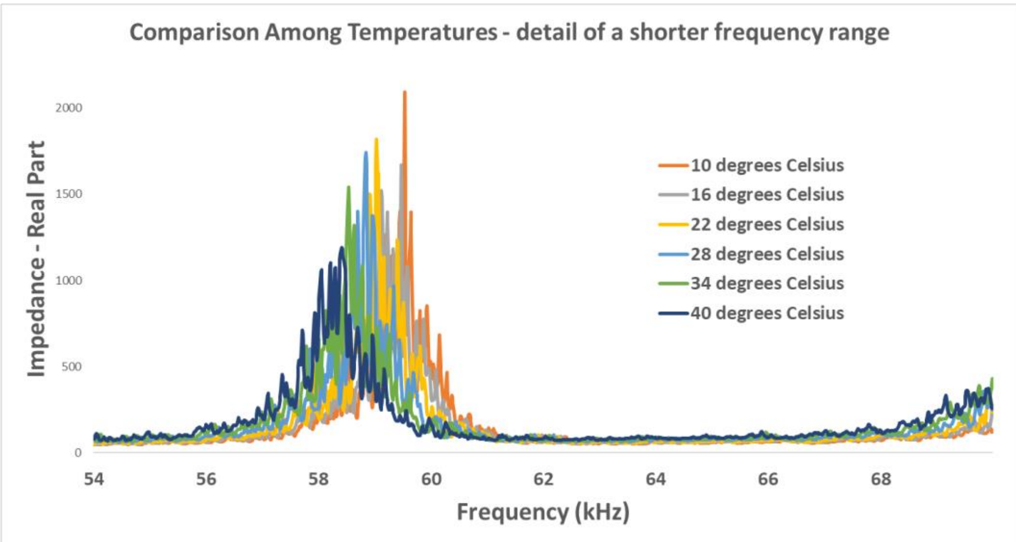

Figure 23: Specimen #1 and temperature changes for Baseline #1- shorter frequency range.

According to the detail in this frequency region, the displacement behavior in the frequency of the impedance peaks is more evident due to the temperature effect. Since the damage metrics work with the comparative calculation between the baseline signal and the monitoring signature, false positives and negatives can occur if there is no such concern with temperature. This can get worse if the threshold on the damage metric is small and measurements take place in very sudden temperature changes.

Figure 24 presents the final objective of monitoring the integrity of a structure, which is to visualize the variations in the impedance curve that are generated due to the process of loss of thickness located in the beam.

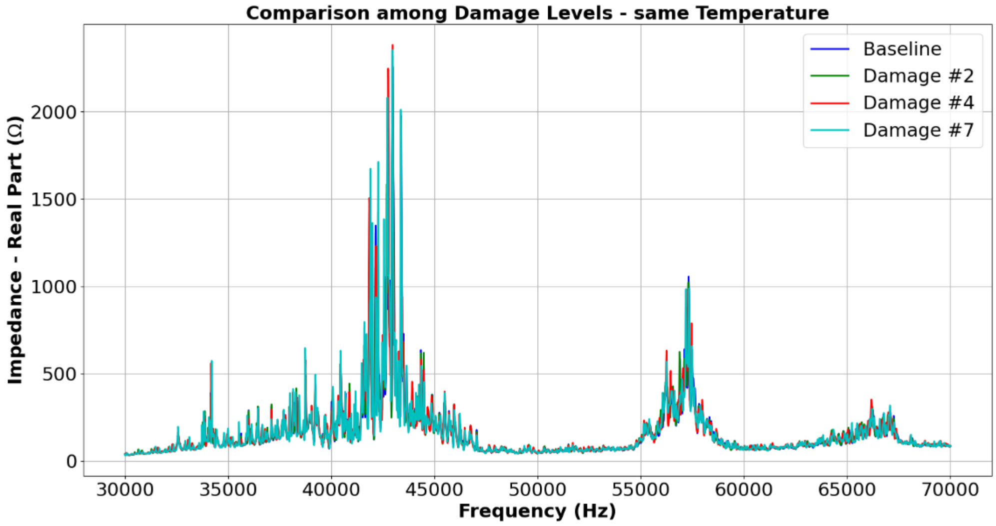

Figure 24: Specimen #1 in the same temperature but different damage conditions.

Again, only a few damage conditions are presented to support understanding of the phenomenon. However, it is possible to see from the image that the variations introduced by the damage are subtle and in specific regions.

Then, for metric calculations, only the set of 30 signatures from Baseline #1 was used. Figure 25 shows the RMSD damage metric for some individual subscriptions under the listed conditions.

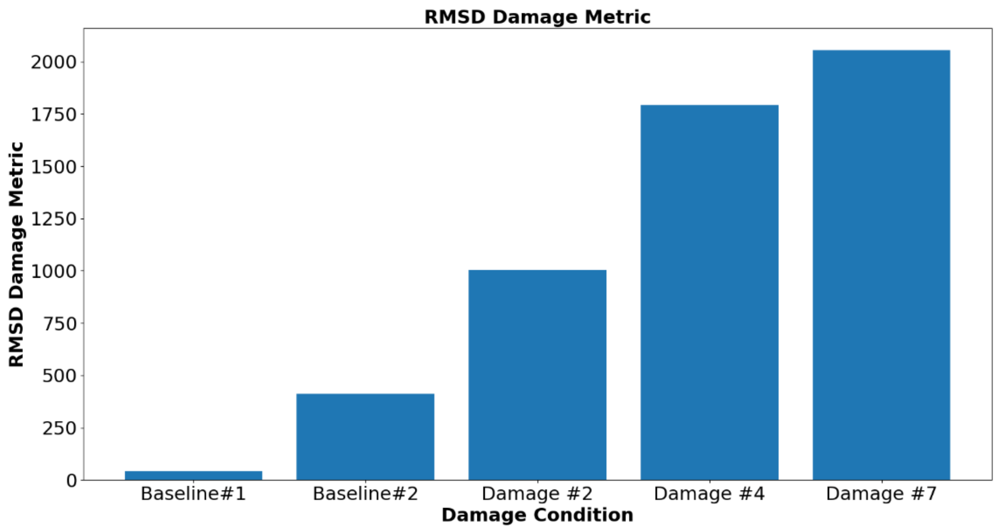

Figure 25: Specimen #1 and some RMSD damage metrics.

According to the figure, it is possible to see a non-null value for Baseline #1 because the comparative calculation of each signature is performed with the median of the 30 signatures of Baseline #1. So, while Baseline #1's damage metric value represents the deviation from the first measurement with its 30-repeat set, Baseline #2 presents the deviation between a measurement from the second reference group and the median of the first reference group.

Figure 26 presents the CCD damage metric. In it, it is possible to see better robustness making the Baseline #1 value practically null. In cases where a greater influence of temperature is perceived, this damage metric has been preferred over other damage metrics.

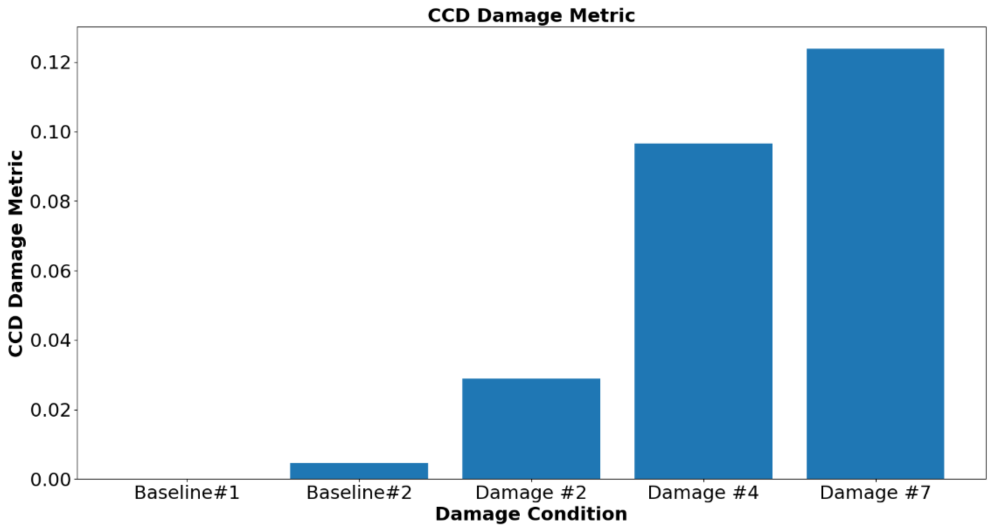

Figure 26: Specimen #1 and some CCD damage metrics.

It is important to note that the threshold value in fault detection needs to be considered around a safety margin. Likewise, the survey of a baseline signature must consider several measurement cycles, not just one with several repetitions. This expands the generalizability. Still, as seen, it is necessary to have baseline measurements at different temperature levels so that it is possible to apply adjustment techniques and make the fault identification more accurate. Several temperature compensation techniques have been studied over the last decades and recently some techniques based on Deep Learning have successfully managed to process data without temperature adjustment. However, even in these cases, the collection of baselines at different temperature levels is of paramount importance.

1.8. References

Baptista FG, Filho JV (2009) A new impedance measurement system for pzt-based structural health monitoring. *IEEE Instrumentation and Measuring* 58(10):3602-3608. DOI: 10.1109/TIM.2009.2018693.

Baptista, F. G.; Vieira Filho, J.; Inman, D. J. . Time-domain analysis of piezoelectric impedance-based structural health monitoring using multilevel wavelet decomposition. *Mechanical Systems And Signal Processing*, v. 25, p. 1550-1558, 2011.

Bhalla S., Soh, C. K. Electromechanical Impedance Modeling for Adhesively Bonded Piezo-Transducers. *Journal of Intelligent Materials*, 15(12):955-972, 2004. Horizonte Científico, Vol. 3, Nº 2, 2009.

Bitencourt, TF, Steffen Jr. Monitoramento Da Integridade Estrutural De Aeronaves, UFU, 2009.

Cavalini, A. A.; Finzi Neto, R. M.; Steffen Jr, V. Impedance-based fault detection methodology for rotating machines. *Structural Health Monitoring*, v. 1, p. 1, 2014.

Chaudhry, Z., Joseph, T., Sun, F. and Rogers, C. (1995), "Local-Area Health Monitoring of Aircraft via Piezoelectric Actuator/Sensor Patches", *Proceedings of the Smart Structures and Integrated Systems 1995*, San Diego-CA, USA, March.

Chaudhry, Z., Lalande, F., Ganino, A., Rogers, C., 1996, "Monitoring the Integrity of Composite Patch Structural Repair via Piezoelectric Actuators/Sensors", AIAA-1996-1074-CP

Finzi Neto, R. M.; Steffen, V.; Rade, D. A.; Gallo, C. A.; Palomino, L. V. . A low-cost electromechanical impedance-based SHM architecture for multiplexed piezoceramic actuators. *Structural Health Monitoring*, v. 1, p. 1-1, 2010.

Ferreira, de Rezende, S. W. F.; Moura Jr, J. R. V.; Finzi Neto, R. M.; Gallo, C. A.; Steffen Jr, V. . Convolutional neural network and impedance-based SHM applied to damage detection. *Engineering Research Express*, v. 1, p. 49-54, 2020.

Freitas, F.A; Jafelice, R.M; Silva, J.W; Rabelo, D.S; Nomelini, Q.S.S; Moura Jr, J.R.V; Gallo, C.A; Cunha, M.J; Ramos, J.E. A new data normalization approach applied to the electromechanical impedance method using adaptive neuro-fuzzy inference system. *Journal of the Brazilian Society of Mechanical Sciences and Engineering*, 43:475, 2021.

Gonçalves, D.R; Moura Jr., J.R.V; Pereira, P.E.C.; Mendes, M.V.A; Diniz-Pinto, H.S. Indicator kriging for damage position prediction by the use of electromechanical impedance-based structural health monitoring. *Comptes Rendus. Mécanique*, v. 349, p. 225-240, 2021.

Grisso, B. L., 2005, "Tailoring the Impedance-Based Structural Health Monitoring Technique to Composites and Wireless Systems", 13th March 2005-CMISS.

Grisso, B. L., Inman, D. J. "Temperature corrected sensor diagnostics for impedance-based SHM". *Journal of Sound and Vibration*. Ed. Elsevier. 2009.

Giurgiutiu, V.; Zagrai, A. Damage Detection in Thin Plates and Aerospace Structure with the Electro-Mechanical Impedance Method. *Structural Health Monitoring*. V. 4(2), p. 99-118, 2005.

Giurgiutiu, V. (2014), Structural health monitoring with piezoelectric wafer active sensors, Elsevier Inc, Academic Press, 2nd edition.

Lakshmi, M; Unnikrishnan, L. Kumar, S. Piezoelectric Polymer Composites for Energy Harvesting Applications: A Systematic Review. *Macromolecular Materials and Engineering* 304(1), 2013.

Liang, C., Sun, F.P. and Rogers, C.A. (1994), "Coupled Electromechanical Analysis of Adaptive Material Systems – Determination of the Actuator Power Consumption and System Energy Transfer" *J. Intell. Mater. Syst. Struct.*, **5**, 12-20.

Martins, L. G. A.; Finzi Neto, R. M.; Palomino, L. V.; Steffen Jr, V.; Rade, D. A. . Architecture of a remote impedance-based structural health monitoring system aiming at aircraft. *Journal of the Brazilian Society of Mechanical Sciences and Engineering*, v. XXXIV, p. 200-393, 2013.

Maruo, I. I.; Giachero, G.; Steffen Jr, V.; Finzi Neto, R. M.. Electromechanical Impedance - Based Structural Health Monitoring Instrumentation System Applied to Aircraft Structures and Employing a Multiplexed Sensor Array. *Journal of Aerospace Technology and Management* (Online), v. 7, p. 294-306, 2015.

Menegaz, G. L.; Tsuruta, K. M.; Finzi Neto, R. M.; Steffen Jr, V.; Araujo, C. A.; GUIMARAES, G. . Use of the electromechanical impedance method in the detection of inclusions: application to mammary tumors. *Structural Health Monitoring*, p. 147592171882513-105, 2019.

Moura Jr, J.R.V.; Steffen Jr, V.. Impedance-based Health Monitoring for Aeronautic Structures using Statistical Meta-modeling. *Journal Of Intelligent Material Systems and Structures*, v. 17, p. 1023-1036, 2006.

Nomelini, Q. S. Schroden; SILVA, J. W.; Gallo, C. A.; Finzi Neto, R. M.; Tsuruta, K. M.; MOURA JR, J. V. . Non-parametric Inference Applied to Damage Detection in the Electromechanical Impedance-based Health Monitoring. *International Journal Of Advanced Engineering Research and Science*, v. 7, p. 73-79, 2020.

Palomino, L.V. and Steffen Jr, V., "Damage Metrics associated with Electromechanical Impedance Technique for SHM applied to a Riveted Structure"; *Proc. of the 20th International Congress of Mechanical Engineering*, Gramado, Brazil, November 15-20, 2009

Palomino, L. V.; Moura Jr, J.R.V.; Tsuruta, K.M.; Rade, D.A.; Steffen Jr, V.. Impedance-based health monitoring and mechanical testing of structures. *Smart Structures and Systems*, v. 7, p. 15-25, 2011.

Palomino, L.V.; Tsuruta, K.M.; Moura Jr, J.R.V.; Rade, D.A.; Steffen Jr, V.; Inman, D.J., "Evaluation of the Influence of Sensor Geometry and Physical Parameters on Impedance-Based Structural Health Monitoring"; 2012, *Shock and Vibration*, Vol. 9, Nb. 5, pp. 811-823 (DOI: 10.3233/SAV-2012-0690)

Park, G., Kabeya, K., Cudney, H.H. and Inman, D.J. (1999), "Impedance- Based Structural Health Monitoring for Temperature Varying Applications", *SME Int .Journal. Ser A. Solid Mech. Mater. Eng. Soc. Mech. Engineers*, **42**(2), 249–258.

Park, G., Cudney, H. and Inman, D. J. (2000), "An Integrated Health Monitoring Technique Using Structural Impedance Sensors", *J. Intell. Mater. Syst. Struct.*, **11**(6), 448-455.

Park, G., Cudney, H. and Inman, D.J. (2001), "Feasibility of Using Impedance-Based Damage Assessment for Pipeline Systems", *Earthquake Engng Struct. Dyn.*, **30**, 1463–1474.

Park G, Sohn H, Farrar CR, et al. Overview of piezoelectric impedance-based health monitoring and path forward. *Shock Vib Digest* 2003; 35(6): 451–463.

Rabelo, Steffen Jr, Finzi Neto, R. M. "Impedance-based structural health monitoring and statistical method for threshold-level determination applied to 2024-T3 aluminum panels under varying temperature". *Structural Health Monitoring*. 2016, v1.

Rabelo, D. S.; Hobeck, J. D.; Inman, D. J.; Finzi Neto, R. M.; Steffen Jr, V. . Real-time structural health monitoring of fatigue crack on aluminum beam using an impedance-based portable device. *Journal Of Intelligent Material Systems And Structures*, p. 1045389X1770521-112, 2017(a).

Rabelo, D. S., Tsuruta, K. M., Oliveira, D. D., Cavalini Jr, A. A., Finzi Neto, R. M., Steffen Jr, V. "Fault Detection of a Rotating Shaft by Using the Electromechanical Impedance Method and a Temperature Compensation Approach". *Journal of Non-Destructive Evaluation*. 2017(b).

Silva, R. N. F.; Tsuruta, K. M.; Rabelo, D. S.; Finzi Neto, R. M.; Cavalini Junior, A. A.; Steffen Jr, V. . Impedance-based structural health monitoring applied to steel fiber-reinforced concrete structures. *Journal of the Brazilian Society of Mechanical Sciences and Engineering*, v. 42, p. 383-15, 2020.

Sun, F.P., Chaudhy, Z., Liang and C., Rogers, C.A. (1995), "Truss Structure Integrity Identification Using PZT Sensor–Actuator" *J. Intell. Mater. Syst. Struct.*, **6**, 134-139.

Tseng, K. K-H.; Naidu, A. S. K. Non-parametric damage detection and characterization using smart piezoceramic material. *Journal Smart Material and Structures*. V.11, p. 317-329, 2002.

Tsuruta, K. M.; Finzi Neto, R. M.; Rabelo, D. S.; Cavalini A. A.; Oliveira, D. D.; Steffen Jr, V. . Fault Detection of a Rotating Shaft by Using the Electromechanical Impedance Method and a Temperature Compensation Approach. *Journal of Nondestructive Evaluation*, v. 36, p. 1-13, 2017.